

Counter-helical magnetic flux ropes from magnetic reconnections in space plasmas

Ying-Dong Jia¹, Yi Qi², Xueyi Wang³, Nathan Miles⁴, Christopher T. Russell¹, and H. Y. Wei¹

¹University of California Los Angeles

²University of Colorado Boulder

³Auburn University

⁴Unknown

April 16, 2024

Abstract

Magnetic flux ropes are ubiquitous in various space environments, including the solar corona, interplanetary solar wind, and planetary magnetospheres. When these flux ropes intertwine, magnetic reconnection may occur at the interface, forming disentangled new ropes. Some of these newly formed ropes contain reversed helicity along their axes, diverging from the traditional flux rope model. We introduce new observations and interpretations of these newly formed flux ropes from existing Hall Magnetohydrodynamics model results. We first examine the time-varying local magnetic field direction at the impact interface to assess the likelihood of reconnection. Then we investigate the electric current system to describe the evolution of these structures, which potentially accelerate particles and heat the plasma. This study offers novel insights into the dynamics of space plasmas and suggests a potential solar wind heating source, calling for further synthetic observations.

Hosted file

984370_0_art_file_11773499_s764b0.docx available at <https://authorea.com/users/528397/articles/701149-counter-helical-magnetic-flux-ropes-from-magnetic-reconnections-in-space-plasmas>

Counter-helical magnetic flux ropes from magnetic reconnections in space plasmas

Ying-Dong Jia¹, Yi Qi², Xueyi Wang³, Nathan Miles^{1,4}, C. T. Russell¹, Hanying Wei¹

¹ Department of Earth, Planetary, and Space Sciences, University of California, Los Angeles, CA, USA

² Laboratory for Atmospheric and Space Physics, University of Colorado Boulder, Boulder, CO, USA

³ Physics Department, Auburn University, Auburn, AL, USA

⁴ Cooperative Institute for Research in Environmental Sciences, Boulder, CO

Abstract

Magnetic flux ropes are ubiquitous in various space environments, including the solar corona, interplanetary solar wind, and planetary magnetospheres. When these flux ropes intertwine, magnetic reconnection may occur at the interface, forming disentangled new ropes. Some of these newly formed ropes contain reversed helicity along their axes, diverging from the traditional flux rope model. We introduce new observations and interpretations of these newly formed flux ropes from existing Hall Magnetohydrodynamics model results. We first examine the time-varying local magnetic field direction at the impact interface to assess the likelihood of reconnection. Then we investigate the electric current system to describe the evolution of these structures, which potentially accelerate particles and heat the plasma. This study offers novel insights into the dynamics of space plasmas and suggests a potential solar wind heating source, calling for further synthetic observations.

Plain language summary

This research examines a special type of systematically twisted magnetic fields, known as flux ropes, in the sun's atmosphere, the solar wind, and near planets. This examination brings new understanding of how these special flux ropes emerge from collisions between flux ropes are built on earlier model results. These results use a commonly used simulation tool for large-scale plasmas to study the new ropes formed after two flux ropes are pushed toward each other long enough. In some cases, each of the new ropes may have opposite twists between their two ends. We then examine how the magnetic field changes across the interface during the evolution.

32 Changes in electric currents found in these situations further explain the formation and evolution
33 of the new rope pairs. This examination helps to better understand the behavior of space
34 plasma's heating of the solar wind and its control of space weather.

35

36 Key points:

- 37 ● We examine the interaction of magnetic flux ropes that consist of opposite helicity along
38 their axis using numerical simulations.
- 39 ● We present the evolution of their current system, from which we anticipate a significant
40 amount of energy release.
- 41 ● These structures could be present on the solar surface, in solar wind, and magnetospheres.

42

43 1. Introduction

44 Magnetic flux ropes (MFRs), certain “flux tubes” characterized by systematically twisted
45 magnetic fields, are pervasive in space plasmas across macroscale and mesoscales (e.g., Hu et al.,
46 2018). Their presence extends beyond coronal mass ejections (CMEs) in the corona
47 (Gopalswamy, 2004), to interplanetary CMEs (ICMEs) in the inner heliosphere (Howard et al.,
48 2009) and flux transfer events (FTEs) in planetary magnetospheres (e.g. Jia et al., 2010; Lai et al.,
49 2012; Belenkaya et al., 2013). Despite their wide range of plasma and field parameter values in
50 various environments, many MFRs are thought to originate from magnetic reconnections (e.g.,
51 Russell & Elphic, 1979a; Moore and Labonte, 1980). Once formed, MFRs are stable and
52 typically display a systematic rotation in their magnetic field vectors, a characteristic readily
53 identifiable in in-situ magnetic field data (Burlaga et al., 1981).

54 Magnetic helicity, a measurement of such rotation signatures, quantifies the relationship
55 between the axial and azimuthal fields in MFRs. In space plasmas, helicity is considered as a
56 conserved quantity, even amidst dissipation processes like magnetic reconnection. For instance,
57 the helicity dissipation time in a typical coronal loop exceeds 10^5 years (Berger and Field, 1984).
58 Such a conservation principle has encouraged decades of efforts to compare ICME properties
59 with their associated solar surface regions (Bothmer and Rust, 1997, Ulrich et al., 2018, Pal,
60 2022). In addition, the generation (Forbes and Priest, 1995; Qiu et al., 2007), distribution (see De
61 Keyser et al., 2005, Chapter 8.6), and transport (Berger and Field, 1984; Manchester et al., 2017)
62 of helicity in (I)CMEs have been extensively investigated. When ICMEs pass by Earth, they are

63 believed to significantly affect magnetospheric activities, with such impacts largely dependent on
64 their helicity (e.g., McAllister 2001).

65 In Earth's magnetosheath, the disentanglement process of colliding MFRs has been observed
66 in Magnetospheric Multiscale (MMS) data (e.g. Qi et al., 2020), resolving a long-standing issue
67 concerning the evolution of interlaced MFRs (e.g. Hesse et al., 1990). Back to the interplanetary
68 space, similar processes are then hypothesized to explain Magnetic Increases with Central
69 Current Sheets (MICCSs) by Fargette et al., (2021). Subsequently, numerical models have been
70 developed to simulate MFR collisions, successfully replicating these disentanglement processes
71 in both the magnetosphere and interplanetary solar wind (Jia et al., 2021; 2023). In some of these
72 model results, we noticed the formation of a new type of MFRs containing the helicity of
73 opposite signs along a single rope, namely counter-helical MFRs (CHFRs). This phenomenon is
74 determined by the initial chirality of these colliding MFR pairs and the local plasma conditions at
75 the interface.

76 On the solar surface, the existence of CHFRs can be found in some numerical simulation
77 results but not thoroughly examined (Linton et al., 2001; Torok et al., 2011). They are also
78 proposed for some erupting CMEs, as inferred from spacecraft imagery (Thompson, 2013).
79 Nonetheless, due to their unstable nature and scarcity of concurrent observations to date,
80 extensive studies of MFRs with differing helicities in the solar wind and magnetospheres have
81 been limited, except for erosion studies (e.g. Pal et al., 2021), prompting a synthetic investigation.

82 In section 2, we reexamine prior numerical models and their outcomes to introduce a
83 particular type of formation of CHFR mechanisms. We detail the magnetic field configurations
84 during their formation process to evaluate the conditions necessary for their production during
85 such processes. In section 3, we analyze the evolution of the associated current system and
86 estimate the energy release of CHFRs. By analyzing various interaction scenarios, our
87 comprehensive study substantiates the formation and evolution of CHFRs. We also highlight
88 their significance and advocate for further observational research in the solar wind and
89 magnetospheres.

90

91 2. Model and results

92 A pair of interlaced flux ropes (IFRs) within the context of a typical 1 AU solar wind is
93 adopted as the initial condition in our time-dependent interaction model. The solar wind

94 parameters are listed in Table 1. Each MFR is formulated by the force-free cylindrical model
 95 (Lundquist, 1950):

$$96 \quad B_r=0, B_{\phi'} = HB_0J_1(\alpha r'/R_0), B_z = B_0J_0(\alpha r'/R_0) \text{ when } r' \leq R_0$$

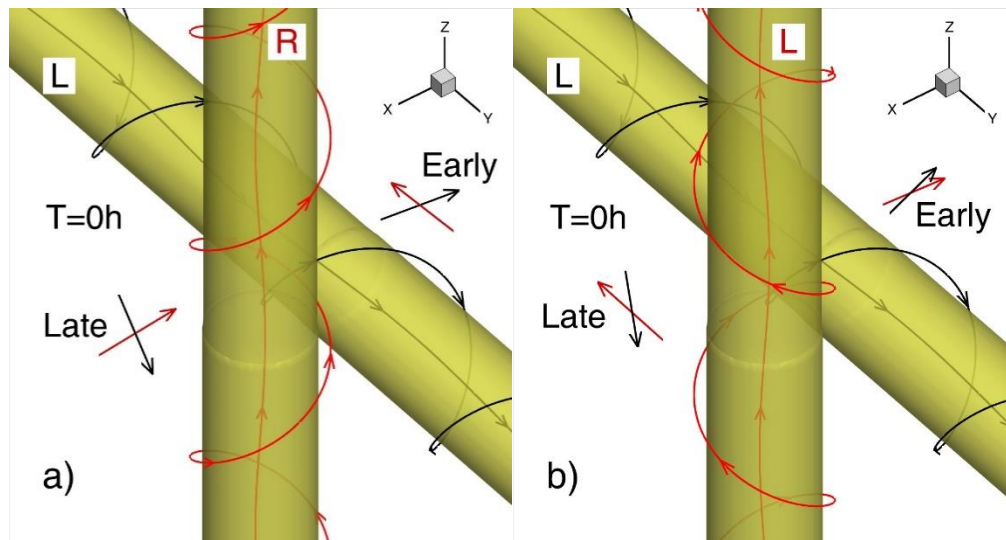
$$97 \quad B = 0 \text{ when } r' > R_0 \quad (1)$$

98 Here, r' , ϕ' , and z' represent local poloidal coordinates centered at the MFR. Functions J_0 and
 99 J_1 are the 0th and 1st-order Bessel functions, respectively. Constant $R_0 = 130\text{Mm}$ is the radius of
 100 the MFR, and the constant $\alpha = 2.405$ is the first 0 point of J_0 , dropping the axial field to zero at
 101 the MFR surface. These components are then transferred into B_x , B_y , and B_z in the Cartesian
 102 coordinate of the simulation domain, as shown in Figure 1. The rope axis z' is set parallel to the
 103 z -axis for the left MFR (initial displacement $x_{L0} = 160\text{Mm}$) and to the y -axis for the right MFR
 104 ($x_{R0} = -160\text{Mm}$), causing an impact angle of 90° . Comparable to the background interplanetary
 105 magnetic field (IMF), we set the axial field $B_0 = 13\text{nT}$. The parameter $H=\pm 1$ denotes the chirality
 106 of the helical magnetic vectors of each MFR: When $H = 1$, the MFR is right-handed.

107 During the evolution, it is anticipated that the plasma flow will drive the two MFRs to
 108 collide, creating an interface at the origin, as depicted in Figure 4 by Jia et al. (2021). For the two
 109 MFRs to successfully disentangle, magnetic reconnection must occur rapidly at this interface.
 110 When variations in other factors are negligible, the rate between the guide field and the
 111 reconnecting field has been found to govern the efficiency of magnetic reconnections using
 112 models and lab experiments (Pritchett & Coroniti, 2004; Lu et al., 2011; Tharp et al., 2012). We
 113 note that the difficulty of verifying this trend with space measurements is reviewed by Genestreti
 114 et al. (2018).

115 To assess the guide field and thereby the likelihood of MFR reconnection, we examine the
 116 magnetic field across the interface before presenting the self-consistent simulation results. In our
 117 conceptualization, we assume that the two MFRs move with the driving plasma flow and
 118 interpenetrate, without experiencing deceleration or deformation. As they overlap, different parts
 119 of the MFRs reach the interface at various stages: The side with the smallest x -coordinate of the
 120 MFR on the left will arrive early, while the part with the largest x -coordinate in this MFR will
 121 arrive later (red arrows in Figure 1). Under this assumption, we use the local field within the
 122 MFRs to depict the field arrows across the interface. Both the early (before reconnection) and
 123 late (after reconnection) stages of this hypothetical interpenetration are sketched in the same 3-D
 124 projection in Figure 1.

125 At the early stage of the hypothetical collision, the magnetic fields in the L-R case (Figure
 126 1a) exhibit a large shear angle, promoting reconnection. In contrast, the magnetic field vectors in
 127 the L-L case (Figure 1b) are nearly parallel, leading to a strong guide field that hinders
 128 reconnection. Conversely, in the later stages of these IFRs, both cases exhibit a significant angle
 129 between field vectors, potentially facilitating reconnection.



130

131 **Figure 1.** Three-dimensional view of the initial conditions ($T=0h$) of two distinct simulation
 132 cases. The black and red curves represent magnetic field lines, spiraling around the yellow
 133 cylinders representing the MFRs. Chirality in the MFRs (L-R, L-L) is indicated by the letters
 134 labeled. After this $T=0$ stage, field arrows are sketched during a hypothetical interpenetration.
 135 Black arrows represent B vectors from the left MFR side ($x < 0$ initially), while red arrows are
 136 from the right MFR ($x > 0$ at $T=0$).

137

138 Two plasma flows, each with a speed of $u = u_x = \pm 13$ km/s, are driven against each other,
 139 maintained by boundary conditions, as shown by the color contours in Figure 2. A 3-D Hall
 140 MHD version (Toth et al., 2008) of the BATS-R-US code (Toth et al., 2012) is used to simulate
 141 this process. Additional details regarding the L-R case, employing the same solar wind condition,
 142 are provided in a recently submitted paper focusing on enhancements in the interplanetary
 143 magnetic field (Jia et al., 2023).

144

145 Table 1. Selection of parameters in models for two distinct space plasma regimes.

	Solar wind	Magnetosheath
n (/cc)	5	10
T (K)	5e5	2e7
B_0 (nT)	12	29
Domain size X_{\max} (Mm)	2000	160
Grid size Dx (Mm)	16	0.3
MFR radius R_0 (Mm)	130	2.5
Time For L-R case to disentangle	17h	40 min

146

147 The solar wind IFR model results with the L-R and L-L configurations are illustrated in Fig.
 148 2. Panels a and b show the evolution of the L-R case. At $T=10$ h, a pair of new MFRs is forming
 149 when left-handed MFRs are connecting to right-handed MFRs. At $T=17$ hours shown in Fig. 2b,
 150 the pair of new MFRs are liberated, each having opposite helicity on their two ends, to form a
 151 pair of CHFRs as sketched in panel c.

152 In contrast, the L-L case shown in panel d remains entangled at 17h, due to the strong guide
 153 field at its early stage. Additional simulations were conducted with varying plasma temperatures
 154 between 5e5 and 1e7 K for this L-L case, but disentanglement did not occur in any of these
 155 scenarios. The outcome of both cases is consistent with our earlier field vector analysis of the
 156 early stage shown in Figure 1.

157

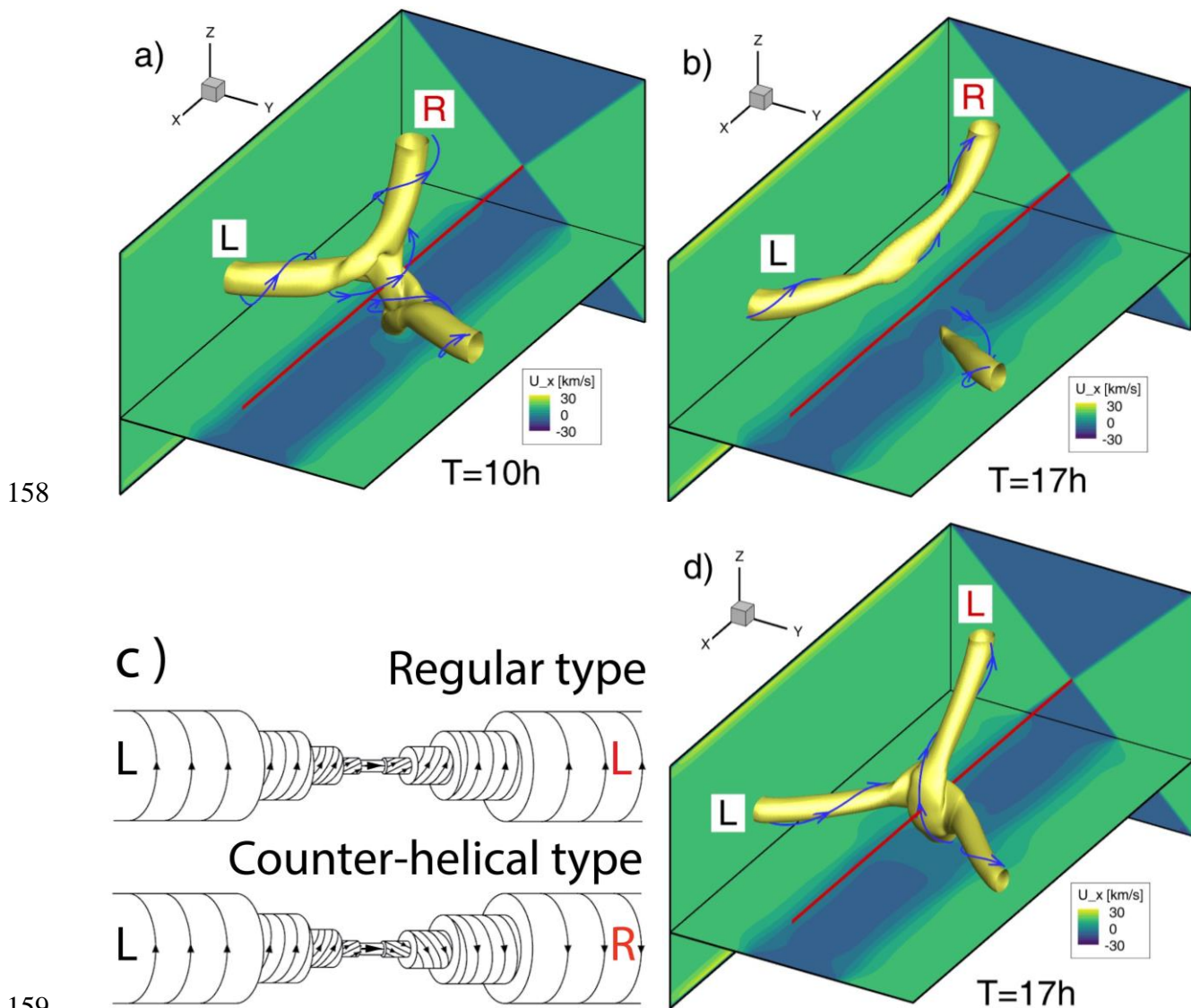


Figure 2. Three-dimensional plots comparing the simulation results of L-R (panels a, b) and L-L (panel d) cases. Panels a and b show the same model result plotted in their Figure 4 by Jia et al. (2023). The blue curves depict field lines winding around the yellow cylinders that represent the MFRs. Color contours illustrate the ion speed component u_x are located at planes defined by $x = -2000$, $y = -1000$, and $z = -360$ Mm, respectively. The red line in the center denotes the x-axis. Panel c sketches a counter-helical MFR and compares it with a regular MFR reproduced from Fig.3 by Russell and Elphic (1979b).

Utilizing the same code, Jia et al. (2021) simulated a comparable process in the Earth's magnetosheath, with the corresponding parameters also detailed in Table 1. Disentanglement

170 occurred in both the L-R and L-L cases. However, the disentanglement process took over 100
 171 minutes for the L-L case, whereas it only required 40 minutes for the L-R case, also consistent
 172 with our vector analysis. To explore kinetic effects during this process, we subsequently
 173 replicated the L-R case in the magnetosheath using a hybrid code (Wang et al., 2009), yielding
 174 consistent results (not shown here). We advocate for additional simulations employing these
 175 computationally intensive kinetic codes to improve the accuracy of our magnetic reconnection
 176 modeling.

177

178 3. Discussion and conclusions

179 Along the axis of an MFR, the axial field's polarity remains constant due to the solenoidal
 180 nature of the magnetic field vector \mathbf{B} . In our IFR scenario, this principle dictates the linkage in
 181 the new pair of MFRs: A disconnected half of the original MFR must pair with the MFR half that
 182 contains the same axial field. For a L-R case, the $-y$ half must connect to the $+z$ half, instead of
 183 the $-z$ half. Consequently, the segments of opposite helicity are connected. Helicity is also an
 184 indicator of another solenoidal vector: The electric current density vector \mathbf{j} (Russell and Elphic,
 185 1979b). For this L-R case, we are thus faced with an apparent dilemma: How do these pairs of
 186 half MFRs carrying opposite \mathbf{j} connect, without violating the divergence-free requirement of \mathbf{j}
 187 under MHD assumptions? To resolve this, we examine these current systems.

188 The left panel of Figure 3 shows the initial current system of MFRs in the L-R case,
 189 calculated from the analytical force-free solution (equation 1). The y -component of current is
 190 plotted in color contours on the two plane slices, with the black curves marking $j_y = 0$. At $x < 0$ as
 191 an example, the radius of the outer black curve is R_0 , which coincides with the MFR radius. The
 192 radius of the inner circle is $r_1 = 1.841R_0/\alpha$, corresponding to the first peak of the Bessel function
 193 $J_1(r')$. As shown on both planes, $j_y > 0$ when $r_1 < r' < R_0$ in a surface region, and $j_y > 0$ when $0 < r'$
 194 $< r_1$ in the core region, indicating the reversal of the axial component of the current in this MFR.

195 We further illustrate this current system in 3-D with color-coded streamlines. This current
 196 reversal is further illustrated by the two colors assigned to the streamlines of \mathbf{j} , differentiating the
 197 surface current from the core current. In the case of the right-handed MFR at $x > 0$, the core
 198 current has the same sign as the poloidal field B_y (white lines), while the surface \mathbf{j} has the
 199 opposite sign (cyan line). This r' -sign relationship inverts when $H = -1$, in the left-handed MFR
 200 at $x > 0$. On the other hand, we note that although the surface current is clustered in a thin layer to

201 compensate for all the core current, their directions still satisfy the $\mathbf{j} = c\mathbf{B}$ nature of a force-free
 202 field: $\mathbf{j}(R0) = \mathbf{j}_\phi$ (not shown), where c is a scalar.

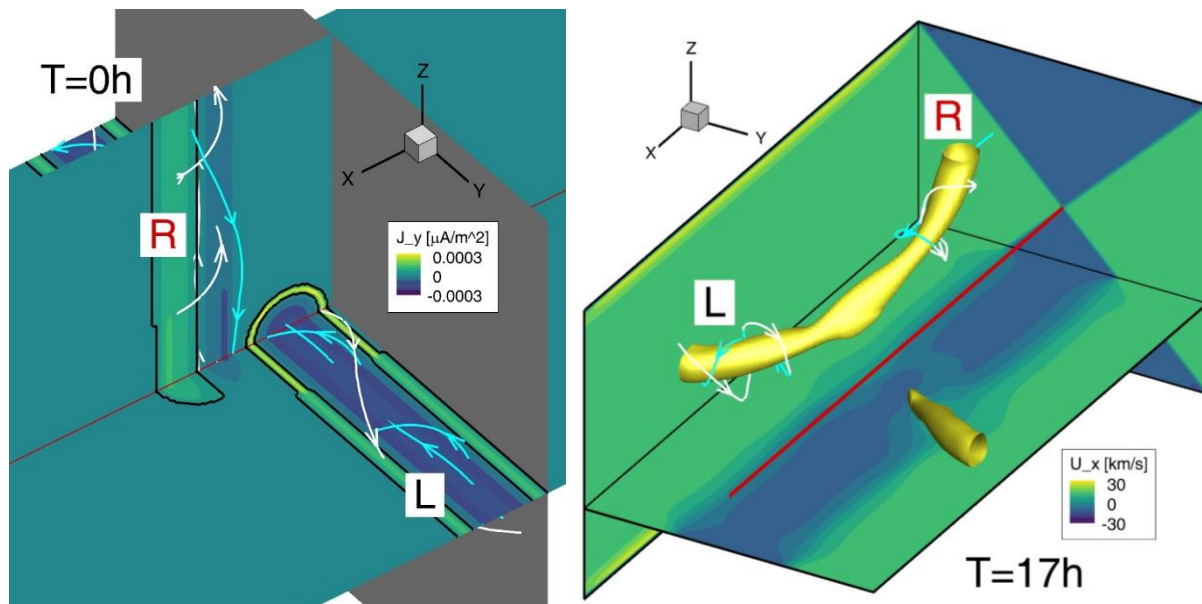
203 Such a surface-core current system occurs because the total current flux in a force-free MFR
 204 equals zero (Solov'ev & Kirichek, 2021), a characteristic also derivable from our Eq. 1.

205 Consequently, when a counter-helical flux rope (CHFR) forms, these currents can close at any
 206 cross-section by connecting the two oppositely flowing currents to conserve the total current flux.

207 This is illustrated by the two self-winding curves in the right panel of Figure 3, which shows the
 208 later stage of the disentanglement process. In the left-handed segment, the surface current (white)
 209 flows in the axial \mathbf{B} direction and then connects to the core current that flows backward (cyan).

210 In summary, this $\nabla \cdot \mathbf{j} = 0$ dilemma is resolved by the self-closure of surface and core currents in
 211 such originally force-free structures.

212



213

214 **Figure 3.** Three-dimensional plots of the L-R case result, with the red lines marking the x-axis.

215 The initial condition is shown in the left panel, with the color contour of the electric current
 216 density j_y component on the $y=0$, and $z=0$ planes. The current $j_y = 0$ along the black lines, with
 217 kinks indicating changes in grid resolution. A gray plane is positioned at $x = -320$ Mm. The
 218 colored curves are current streamlines in 3-D: When the polarity of \mathbf{j} is the same as the magnetic
 219 field ($\mathbf{j} \cdot \mathbf{B} > 0$), it's colored in cyan, and white for opposite polarity ($\mathbf{j} \cdot \mathbf{B} < 0$). The right panel

220 displays the same result at $T=17h$ as shown in Figure 2b. However, electric current lines are
221 plotted here instead of magnetic field lines.

222

223 In the middle of such a new CHFR, the magnetic field is predominantly poloidal, rendering
224 the axial current negligible, and this region is no longer force-free. Thus, CHFRs are not stable
225 and will dissipate. Starting from the center and propagating to both ends, the current system will
226 rearrange. Correspondingly, the azimuthal magnetic field will gradually align towards the axial
227 field. Ideally, the opposite helicity will annihilate, and a CHFR becomes a magnetic flux tube
228 without any twist in its field. This annihilation will release all the energy of the azimuthal
229 component of the magnetic field, which is about $1/6$ of the total magnetic energy, as can be
230 integrated from equation 1. Although this release occurs over an extended period, this amount of
231 energy discharged from the entire MFR is orders of magnitude larger than that produced during
232 the reconnection at the impact interface. This energy may contribute to particle acceleration or
233 plasma heating and thus heats the solar wind. In the tranquil solar wind where plasma dynamics
234 are minimal, the propagation speed of this alignment, estimated using the Alfvén speed, is
235 typically below 0.1 times the solar wind speed. Consequently, a CHFR that passes through a
236 detector within one hour, with its poloidal length scale exceeding its cross-section scale (large
237 aspect ratio), could sustain for over 10 hours, offering sufficient opportunity for observation.

238 In our simulations of both the solar wind and magnetosheath environments, we assumed a
239 90° impact angle between the MFRs. This angle affects the relative field orientation across the
240 interaction interface. Utilizing the same vector sketch approach as demonstrated in Figure 1, we
241 find that both L-L and L-R configurations can lead to disentanglement across a range of impact
242 angles, thereby supporting the production of CHFRs from IFRs.

243 Similarly, Linton et al. (2001) investigated MFR interactions in the low corona with a MHD
244 code. They propelled uniformly twisted MFRs (Gold & Hoyle, 1960) in a solenoidal velocity
245 field, achieving a disentanglement process that they call “slingshot”. We note that their product
246 is an R-L CHFR (see their Figure 10). However, their parameters are normalized to magnetic
247 field B_0 and MFR radius R_0 , precluding a direct comparison with our Table 1. CHFRs can be
248 found in their model results for impact angles between 90° and 270° . These results were later
249 confirmed with a zero- β MHD simulation (Torok et al., 2011), to explain an indicated CHFR
250 involved in an eruption on the solar surface (Chandra et al., 2010). On the other hand, most

251 studies on the interaction between MFRs focus on those whose axes are parallel to each other
252 (e.g. Lau and Finn, 1996; Hansen et al., 2004, Zhao et al., 2015) to find multi-point interactions,
253 where CHFRs are not evident.

254 MFRs with asymmetric helicity within their cross-sections have been suggested in the
255 context of CMEs undergoing erosion via magnetic reconnection (Dasso et al., 2006; Pal et al.,
256 2021). Additionally, MFRs with varying helicities along their axes, although unstable, have been
257 proposed based on particle time-of-flight data in ICMEs (Cane et al., 1997; Owens et al., 2016).
258 A recent multi-spacecraft observation, despite certain uncertainties, found opposite helicity from
259 different parts of an ICME (Rodríguez-García et al., 2022). We recommend further examination
260 of such cases because CHFR is a plausible, likely, and important phenomenon. Such
261 investigations would expand our knowledge of MFRs in space plasmas.

262 The curvature and activities in the magnetosheath make MFRs complex and transient (e.g.
263 Chen et al., 2017; Guo et al., 2021). Still, it's possible for one or a few spacecraft to cross the
264 same curved MFR at different locations. When a spacecraft detects two shortly separated MFRs
265 with identical plasma content but measures opposite chirality, it may be seeing a newly formed
266 CHFR, providing another chance to observe CHFRs.

267 IFRs, a prerequisite condition for CHFRs generated in this study, are commonly observed in
268 the inner heliosphere (Qi et al., 2020; Fargette et al., 2021). Additionally, the mixing of MFRs
269 with opposite helicities, another condition for such CHFRs to form, is also available for small-
270 scale MFRs in the solar wind (Zhao et al., 2021). However, identifying variable helicity along an
271 MFR is challenging, given the determination of helicity from a single spacecraft measurement is
272 notoriously challenging (Hu, 2017). Additionally, the concept of multiple MFRs winding around
273 each other (Hu et al., 2004; Hwang et al., 2021, Figure 1e), MFRs with opposite helicity within
274 their cross sections (Florido-Llinas et al., 2020), and MFR distortion (Nieves-Chinchilla et al,
275 2023) has been proposed, further acknowledging the complexity of MFRs in observation data.
276 Nevertheless, with the increasing number of probes in the inner heliosphere, CHFRs may be
277 observable through coherent observations from multiple spacecraft. Alternative methods of
278 identification are also possible, like solar images (e.g. Zhang et al., 2012) and hints from in situ
279 plasma data.

280 In addition to IFRs, direct emergence from the solar surface to generate CHFRs has been
281 proposed when analyzing vector magnetograms (Vemareddy, 2021). Are there other processes to

282 form CHFRs in the solar wind? How often are they generated? More investigation is needed to
283 answer such questions.

284 In summary, CHFRs have been identified in previous research, but their discussion has not
285 been exhaustive. Focusing on a specific generation mechanism, we show the details of such
286 structures to affirm their existence and highlight their significance. Additional theoretical and
287 observational efforts are necessary across various regions of the inner heliosphere to comprehend
288 the stability, evolution, and propagation of CHFRs. This study is significant for advancing our
289 knowledge in solar wind heating and space weather, given the energy CHFRs release and the
290 north-south magnetic flux they carry.

291

292 Acknowledgment

293 We acknowledge support from STEREO NASA award number 80NSSC21K1512, and MMS award
294 number NNG04EB99C.

295

296 Data Availability Statement

297 The BARS-R-US code used in the study is available for download as a component of the Space
298 Weather Modeling Framework at the University of Michigan
299 (<http://clasp.engin.umich.edu/swmf>).

300

301

302 References

- 303 Belenkaya, E. S., Alexeev, I. I., Slavin, J. A., and Blokhina, M. S. (2013), Influence of the solar
304 wind magnetic field on the Earth and Mercury magnetospheres in the paraboloidal model,
305 Planet. Space Sci., 75, 46–55, DOI: 10.1016/j.pss.2012.10.013
- 306 Berger, M. A., Field, G. B. (1984), The topological properties of magnetic helicity, Journal of
307 Fluid Mechanics, 147, DOI: <https://doi.org/10.1017/S0022112084002019>
- 308 Bothmer, V., Rust, D. M. (1997), The Field Configuration of Magnetic Clouds and the Solar
309 Cycle, Geophysical Monograph Series 99, Coronal Mass Ejections,
310 <https://doi.org/10.1029/GM099p0139>
- 311 Burlaga, L. ; Sittler, E. ; Mariani, F. ; Schwenn, R. (1981), Magnetic loop behind an
312 interplanetary shock: Voyager, Helios, and IMP 8 observations, Journal of Geophysical
313 Research, 86(A8), p. 6673-6684, DOI: 10.1029/JA086iA08p06673
- 314 Cane, H. V., Richardson, I. G., Wibberenz, G. (1997), Helios 1 and 2 observations of particle
315 decreases, ejecta, and magnetic clouds, J. Geophys. Res., 102, A4,
316 <https://doi.org/10.1029/97JA00149>
- 317 Chandra, R., Pariat, E., Schmeider, B., Mandrini, C. H., Uddin, W. (2010), How Can a Negative
318 Magnetic Helicity Active Region Generate a Positive Helicity Magnetic Cloud? Solar
319 Phys., 261, doi:10.1007/s11207-009-9470-2.
- 320 Chen, Y., Tóth, G., Cassak, P. et al. (2017), Global three-dimensional simulation of Earth's
321 dayside reconnection using a two-way coupled magnetohydrodynamics with embedded
322 particle-in-cell model: Initial results. Journal of Geophysical Research: Space Physics, 122,
323 10,318–10,335. <https://doi.org/10.1002/2017JA024186>
- 324 Dasso, S., Nakwacki, M. S., Démoulin, P. et al. (2006), A new model-independent method to
325 compute magnetic helicity in magnetic clouds, Astronomy and Astrophysics, Volume 455,
326 Issue 1, DOI: 10.1051/0004-6361:20064806
- 327 De Keyser, J., M. W. Dunlop, C. J. Owen, B. U. Ö. Sonnerup, S. E. Haaland, A. Vaivads, G.
328 Paschmann, R. Lundin, and L. Rezeau (2005), Magnetopause and boundary layer, Space
329 Sci. Rev., 118, 231–320, doi:10.1007/ s11214-005-3834-1
- 330 Fargette, N., Lavraud, B., Rouillard, A., et al. (2021). Magnetic increases with central current
331 sheets: observations with Parker Solar Probe. Astronomy & Astrophysics, 650(A11).
332 <https://doi.org/10.1051/0004-6361/202039191>

- 333 Florido-Llinas, M., Nieves-Chinchilla, T., Linton, M. G. (2020), Analysis of the Helical Kink
334 Stability of Differently Twisted Magnetic Flux Ropes, *Solar Phys.*, 295(9), DOI:
335 10.48550/arXiv.2007.06345
- 336 Forbes, T. G., Priest, E. R. (1995), Photospheric Magnetic Field Evolution and Eruptive Flares,
337 *Astrophys. J.*, 446, DOI: 10.1086/175797
- 338 Genestreti, K. J., Nakamura, T. K. M., Nakamura, R., E. R. et al. (2018), How Accurately Can
339 We Measure the Reconnection Rate EM for the MMS Diffusion Region Event of 11 July
340 2017? *J. Geophys. Res.*, 123, A11, DOI: 10.1029/2018JA025711
- 341 Gold T., F. Hoyle, On the Origin of Solar Flares, *Monthly Notices of the Royal Astronomical*
342 *Society*, Volume 120, Issue 2, February 1960, Pages 89–105,
343 <https://doi.org/10.1093/mnras/120.2.89>
- 344 Gopalswamy, N. (2004). A Global Picture of CMEs in the Inner Heliosphere. In: Poletto, G.,
345 Suess, S.T. (eds) *The Sun and the Heliosphere as an Integrated System*. Astrophysics and
346 *Space Science Library*, vol 317. Springer, Dordrecht. [https://doi.org/10.1007/978-1-4020-](https://doi.org/10.1007/978-1-4020-2831-1_8)
347 [2831-1_8](https://doi.org/10.1007/978-1-4020-2831-1_8)
- 348 Guo, Z., Lin, Y., & Wang, X. (2021). Global hybrid simulations of interaction between
349 interplanetary rotational discontinuity and bow shock/magnetosphere: Can ion-scale
350 magnetic reconnection be driven by rotational discontinuity downstream of quasi-parallel
351 shock? *Journal of Geophysical Research: Space Physics*, 126, e2020JA028853.
352 <https://doi.org/10.1029/2020JA028853>
- 353 Hansen, J. F., Tripathi, S. K. P., Bellan, P. M. (2004), Co- and counter-helicity interaction
354 between two adjacent laboratory prominences, *Phys. Plasmas*, 11.
355 <https://doi.org/10.1063/1.1724831>
- 356 Hesse, M., Birn, J., & Schindler, K. (1990), On the topology of flux transfer events. *Journal of*
357 *Geophysical Research*, 95(A5), 6549. <https://doi.org/10.1029/ja095ia05p06549>
- 358 Howard, T.A., Tappin, S.J. (2009), Interplanetary Coronal Mass Ejections Observed in the
359 Heliosphere: 1. Review of Theory. *Space Sci Rev* 147, 31–54
360 <https://doi.org/10.1007/s11214-009-9542-5>
- 361 Hu, Q., C. W. Smith, N. F. Ness, and R. M. Skoug (2004), Multiple flux rope magnetic ejecta in
362 the solar wind, *J. Geophys. Res.*, 109, A03102, doi:10.1029/2003JA010101.

- 363 Hu, Q. The Grad–Shafranov Reconstruction of Toroidal Magnetic Flux Ropes: Method
364 Development and Benchmark Studies. *Sol Phys* 292, 116 (2017).
365 <https://doi.org/10.1007/s11207-017-1134-z>
- 366 Hu, Q., Zheng, J., Chen, Y., Roux, J., & Zhao, L. (2018). Automated Detection of Small-scale
367 Magnetic Flux Ropes in the Solar Wind: First Results from the Wind Spacecraft
368 Measurements. *The Astrophysical Journal Supplement Series*, 239(1).
369 <https://doi.org/10.3847/1538-4365/aae57d>
- 370 Hwang, K.-J., Burch, J. L., Russell, C. T. et al. (2021), Microscale Processes Determining
371 Macroscale Evolution of Magnetic Flux Tubes along Earth's Magnetopause, *Astrophys. J.*,
372 914, 1, DOI 10.3847/1538-4357/abf8b1
- 373 Jia, X., Walker, R. J., Kivelson, M. G., et al. (2010), Dynamics of Ganymede's magnetopause:
374 Intermittent reconnection under steady external conditions, *J. Geophys. Res.*, 115, A12,
375 <https://doi.org/10.1029/2010JA015771>
- 376 Jia, Y.-D., Qi, Y., Lu, S., & Russell, C. T. (2021). Temporal evolution of flux rope/tube
377 entanglement in 3-D Hall MHD simulations. *Journal of Geophysical Research: Space*
378 *Physics*, 126, e2020JA028698. <https://doi.org/10.1029/2020JA028698>
- 379 Jia, Y.-D., Hairong Lai, Nathan Miles, et al. (2023), Magnetic Field Enhancements in the
380 Interplanetary Solar Wind: Diverse Processes Manifesting a Uniform Observation Type?.
381 ESS Open Archive, DOI: 10.22541/essoar.170110674.49544737/v1
- 382 Lai, H. R., H. Y. Wei, C. T. Russell, C. S. Arridge, and M. K. Dougherty (2012), Reconnection
383 at the magnetopause of Saturn: Perspective from FTE occurrence and magnetosphere size,
384 *J. Geophys. Res.*, 117, A05222, doi:10.1029/2011JA017263.
- 385 Lau, Y.-T., Finn, J. M. (1996), Magnetic reconnection and the topology of interacting twisted
386 flux tubes, *Physics of Plasmas*, 3(11), DOI: 10.1063/1.871571
- 387 Linton, M. G., Dahlburg, R. B., & Antiochos, S. K. (2001). Reconnection of twisted flux tubes as
388 a function of contact angle. *The Astrophysical Journal*, 553(2), 905–921.
389 <https://doi.org/10.1086/320974>
- 390 Lundquist S (1950) Magneto-hydrodynamic fields. *Ark Fys* 2:361–365
- 391 Lu, S., Lu, Q. M., Cao, Y. et al. (2011), The effects of the guide field on the structures of
392 electron density depletions in collisionless magnetic reconnection, *Chinese Sci. Bull*, 56,
393 issue 1, DOI: 10.1007/s11434-010-4250-9

- 394 Manchester, W., Kilpua, E.K.J., Liu, Y.D. et al. The Physical Processes of CME/ICME
395 Evolution. *Space Sci Rev* 212, 1159–1219 (2017). [https://doi.org/10.1007/s11214-017-](https://doi.org/10.1007/s11214-017-0394-0)
396 [0394-0](https://doi.org/10.1007/s11214-017-0394-0)
- 397 McAllister, A. H., Martin, S. F., Crooker, N. U. et al. (2001), A test of real-time prediction of
398 magnetic cloud topology and geomagnetic storm occurrence from solar signatures, *J.*
399 *Geophys. Res.*, 106, A12, <https://doi.org/10.1029/2000JA000032>
- 400 Moore, R. L., LaBonte, B. J. (1980), The filament eruption in the 3B flare of July 29, 1973 -
401 Onset and magnetic field configuration, in *Solar and Interplanetary Dynamics; Proceedings*
402 *of the Symposium, Cambridge, Mass., (A81-27626 11-92)* Dordrecht, D. Reidel Publishing
403 Co., 1980, p. 207-210; Discussion, p. 211.
- 404 Nieves-Chinchilla, T., M. A. Hidalgo, and H. Cremades (2023), Distorted-toroidal Flux Rope
405 Model, *Astrophys. J.*, 947, 79, DOI 10.3847/1538-4357/acb3c1
- 406 Owens, M. J., Forsyth, R. J., Horbury, T. S., et al. (2016), DO THE LEGS OF MAGNETIC
407 CLOUDS CONTAIN TWISTED FLUX-ROPE MAGNETIC FIELDS? *Astrophys. J.*, 818,
408 50, DOI: 10.3847/0004-637X/818/2/197
- 409 Pal, S., Kilpua, R., Good, S. (2021), Uncovering erosion effects on magnetic flux rope twist,
410 *Astron. Astrophys.*, 650, A176, <https://doi.org/10.1051/0004-6361/202040070>
- 411 Pal, S. (2022), Uncovering the process that transports magnetic helicity to coronal mass ejection
412 flux ropes, *Adv. Space Res.*, 70, 6, <https://doi.org/10.1016/j.asr.2021.11.013>
- 413 Pritchett, P. L., and F. V. Coroniti (2004), Three-dimensional collisionless magnetic
414 reconnection in the presence of a guide field, *J. Geophys. Res.*, 109, A01220,
415 doi:10.1029/2003JA009999.
- 416 Qi, Y., Russell, C. T., Jia, Y.-D., & Hubbert, M. (2020). Temporal evolution of flux tube
417 entanglement at the magnetopause as observed by the MMS satellites. *Geophysical*
418 *Research Letters*, 47, e2020GL090314. <https://doi.org/10.1029/2020GL090314>
- 419 Qiu, J., Hu, Q., Howard, T. A., Yurchyshyn, V. B. (2007), On the Magnetic Flux Budget in Low-
420 Corona Magnetic Reconnection and Interplanetary Coronal Mass Ejections, *Astrophys. J.*,
421 659(1), DOI: 10.1086/512060
- 422 L. Rodríguez-García, T. Nieves-Chinchilla, R. Gómez-Herrero et al., (2022), Evidence of a
423 complex structure within the 2013 August 19 coronal mass ejection, *A&A* 662(A45), DOI:
424 <https://doi.org/10.1051/0004-6361/202142966>

- 425 Russell, C. T., Elphic, R. (1979a), ISEE observations of flux transfer events at the dayside
426 magnetopause, *Geophys. Res. Lett.*, 6, 1, DOI: 10.1029/GL006i001p00033
- 427 Russell, C. T., Elphic, R. (1979b), Observation of magnetic flux ropes in the Venus ionosphere,
428 *Nature*, 279, DOI: 10.1038/279616a0
- 429 Solov'ev, A. A., Kirichek, E. A. (2021), Properties of the Flare Energy Release in Force-Free
430 Magnetic Flux Ropes, *Mon. Not. R. Astron. Soc.*, 505,
431 <https://doi.org/10.1134/s1063773723050055>
- 432 Tharp T, Yamada M, Ji H et al. (2012) Quantitative study of guide-field effects on Hall
433 reconnection in a laboratory plasma. *Phys Rev Lett* 109:169002,
434 <https://doi.org/10.1103/PhysRevLett.109.165002>
- 435 Thompson W.T. (2013), Alternating Twist Along an Erupting Prominence, *Solar Phys*, 283:489–
436 504, DOI 10.1007/s11207-013-0228-5
- 437 Torok, T., Chandra, R., Pariat, E. et al. (2011), FILAMENT INTERACTION MODELED BY
438 FLUX ROPE RECONNECTION, *Astrophys. J.*, 728, 65, DOI 10.1088/0004-
439 637X/728/1/65
- 440 Tóth, G., Ma, Y. J., & Gombosi, T. I. (2008). Hall magnetohydrodynamics on block-adaptive
441 grids. *Journal of Computational Physics*, 227(14), 6967–6984.
442 <https://doi.org/10.1016/j.jcp.2008.04.010>
- 443 Tóth, G., van der Holst, B., Sokolov, I. V., De Zeeuw, D. L., Gombosi, T. I., Fang, F., et al.
444 (2012). Adaptive numerical algorithms in space weather modeling. *Journal of*
445 *Computational Physics*, 231(3), 870–903. <https://doi.org/10.1016/j.jcp.2011.02.006>
- 446 Ulrich, R. K., Riley, P., Tran, T. (2018), Solar Sources of Interplanetary Magnetic Clouds
447 Leading to Helicity Prediction, *Space Weather*, 16, 11,
448 <https://doi.org/10.1029/2018SW001912>
- 449 Vemareddy, P. (2021), Successive injection of opposite magnetic helicity: evidence for active
450 regions without coronal mass ejections, *Mon. Not. R. Astron. Soc.*, 507.
451 <https://doi.org/10.1093/mnras/stab2401>
- 452 Wang, X. Y., Lin, Y., & Chang, S.-W. (2009). Hybrid simulation of foreshock waves and ion
453 spectra and their linkage to cusp energetic ions. *Journal of Geophysical Research*, 114(A6),
454 A06203. <https://doi.org/10.1029/2008JA013745>

455 Zhang, J., Cheng, X. & Ding, Md. Observation of an evolving magnetic flux rope before and
456 during a solar eruption. Nat Commun 3, 747 (2012). <https://doi.org/10.1038/ncomms1753>
457 Zhao, L., DeVore, C. R., Antiochos, S. K. (2015), NUMERICAL SIMULATIONS OF
458 HELICITY CONDENSATION IN THE SOLAR CORONA, Astrophys. J., 805:61, DOI
459 10.1088/0004-637X/805/1/61
460 Zhao, L.-L., G. P. Zank, Q. Hu, et al. (2021). Detection of small magnetic flux ropes from the
461 third and fourth Parker Solar Probe encounters. Astronomy & Astrophysics, 650(A12).
462 <https://doi.org/10.1051/0004-6361/202039298>
463